Microtubule re-organization during female meiosis in *C. elegans*

Ina Lantzsch[1], Che-Hang Yu[2], Hossein Yazdkhasti[6], Norbert Lindow[3], Erik Szentgyörgyi[1], Steffen Prohaska[3], Martin Srayko[4], Sebastian Fürthauer[5], and Stefanie Redemann[6]

[1] Experimental Center, Faculty of Medicine Carl Gustav Carus, Technische Universität Dresden, Germany

[2] Department of Electrical and Computer Engineering, University of Carlifornia, Santa Barbara, CA, USA

[3] Zuse Institute Berlin, 14195 Berlin, Germany

[4] Department of Biological Sciences, University of Alberta, Edmonton, Canada

[5] Center for Computational Biology, Flatiron Institute, NY, USA

[6] Center for Membrane and Cell Physiology & Department of Molecular Physiology and Biological Physics, University of Virginia, School of Medicine, Charlottesville, VA, USA

Correspondence to: Stefanie Redemann (sz5j@virginia.edu), Sebastian Fürthauer (sfuerthauer@flatironinstitute.org)

Abstract

The female meiotic spindles of most animals are acentrosomal and undergo drastic morphological changes while transitioning from metaphase to anaphase. The ultra-structure of acentrosomal spindles, and how this enables such dramatic rearrangements remains largely unknown.

To address this, we applied light microscopy, large-scale electron tomography and mathematical modeling of female meiotic *C. elegans* spindles undergoing the transition from metaphase to anaphase. Combining these approaches, we find that meiotic spindles are dynamic arrays of short microtubules that turn over on second time scales. The results show that the transition from metaphase to anaphase correlates with an increase in the number of microtubules and a decrease of their average length. To understand the mechanisms that drive this transition, we developed a mathematical model for the microtubule length distribution that considers microtubule growth, catastrophe, and severing. Using Bayesian inference to compare model predictions and data, we find that microtubule turn-over is the major driver of the observed large-scale reorganizations. Our data suggest that cutting of microtubules occurs, but that most microtubules are not severed before undergoing catastrophe.

Introduction

During meiosis, haploid gametes are produced from diploid progenitor cells in most sexually reproducing eukaryotes. The reduction of chromosome number in the gametes is essential for the development of the fertilized oocyte into an embryo. Therefore, the accuracy of meiosis is crucial, as errors in chromosome segregation result in aneuploidies and lead to genetic disorders, which are often lethal (Hassold & Hunt 2001).

In this paper, we study the structure and dynamics of female meiotic spindles in *C. elegans*. Female meiotic spindles, like mitotic and male meiotic spindles, are built from microtubules (MTs), motor proteins and microtubule-associated proteins. However, unlike other spindles in most animals, female meiotic spindles typically have no centrosomes, due to centriole elimination during oogenesis. Thus, female meiotic spindles are assembled differently from those that rely on centrosome-based microtubule-organizing centers. Specifically, this is true in humans (Holubcová et al., 2015), mice (Schuh and Ellenberg, 2007) and also in nematodes (Albertson and Thomson, 1993). It is an open question how their structure reflects the differences in assembly.

In *C. elegans*, female meiotic spindles undergo a drastic reorganization during the metaphase-to-anaphase transition. During metaphase of meiosis I and II, microtubules form a pointed and elongated bipolar spindle, which then shortens during anaphase. In addition, the microtubule density shifts from the spindle poles to the midzone between the separating chromosomes. This mid-zone then extends until the end of anaphase (Dumont et al., 2010; Laband et al., 2017, Yu et al 2019). The structural basis of these

rearrangements and their role in meiotic chromosome segregation are not well understood. In particular, it remains unclear whether these structural rearrangements are driven by katanin-mediated severing (Joly et al 2016, Srayko et al 2006), transport (Mullen & Wignall 2017, Brugués et al 2012) or changes in MT nucleation or polymerization dynamics (Brugués et al 2012, Needleman et al 2010).

Here, we approach the mechanisms of structural microtubule arrangement by using large-scale electron tomography (Redemann et al 2017 & 2018, Fabig et al 2020) to obtain the 3D ultrastructure of spindles in *C. elegans* oocyte meiosis. We find that the female meiotic spindles are composed of arrays of short microtubules, 90% are shorter than half spindle length, which are highly dynamic and turn-over within 10s. During the transition from metaphase to anaphase, the number and lengths of microtubules change significantly. To understand the drivers of these changes we developed a mathematical model for the length distributions of microtubules that includes life time (turn-over), growth, and microtubule severing. We then compared the model to our data using Bayesian inference and found that the change in microtubule number and lengths is mostly caused by changing microtubule turnover. While severing clearly occurs, our data suggests that it affects only a minor fraction of microtubules during the transition from metaphase to anaphase.

Results

Three-dimensional reconstruction reveals the structural changes of the spindle throughout female meiosis

Previous analyses of meiotic spindle microtubules using EM tomography involved only subsections of the spindle rather than the entire structure, which makes it difficult to measure the total length of microtubules composing the spindle, as most microtubules would be leaving the tomographic volume. We obtained the spindle ultrastructure of *C. elegans* oocytes by serial-section electron tomography, which allows the reconstruction of whole spindles in 3D with single-microtubule resolution (Redemann et al., 2017 & 2018). We reconstructed two meiotic spindles in metaphase I (named metaphase #1 and #2), as well as four spindles at early, mid and late stages of anaphase I (two data sets for late anaphase I, named #1 and #2; Fig. 1A, Suppl. Movie 1-3). In addition, we reconstructed one metaphase, one early anaphase, one mid anaphase and one late anaphase stage of meiosis II oocytes (Suppl. Fig. 1). We had previously analyzed the attachment of microtubules to chromosomes and the role of microtubules in chromosome segregation during anaphase using the Meiosis I metaphase #2, early anaphase, mid anaphase datasets (Redemann et al 2018) and late anaphase (#1) (Yu et al 2019) of the first meiotic division. Here, we used those datasets, as well as newly generated meiosis II datasets to quantitatively characterize the spindle structure and microtubule rearrangements during female meiosis.

For this, we compiled summary statistics that characterize spindle morphology. In Table 1 we report the spindle length, the number of microtubules, the average microtubule length, the maximum microtubule length and the total polymer length for each stage of

meiosis I (Table 1). A similar analysis for meiosis II spindles is given in the supplementary section (see Suppl. Fig. 1B). Since meiosis I and II were not significantly different we focused on meiosis I.

Female meiotic spindles are arrays of short microtubules

We first sought to characterize the overall spindle structure. Female meiotic spindles could be constructed mainly from long microtubules, reaching from near the spindle pole to chromosomes (as in *C. elegans* mitotic spindles; Redemann et al 2017), or from short ones distributed throughout the spindle volume, as suggested by Srayko et al., 2006, and for instance, meiotic *Xenopus* spindles (Brugués et al 2012).

Our data show that throughout meiosis I and meiosis II, roughly 40-50% of microtubules are shorter than 500 nm (Fig. 1B, Suppl. Fig. 1C). In contrast, the fraction of microtubules that are at least half spindle length or longer is only 10%. In metaphase, the average microtubule length is 1 µm ± 0.87 µm (mean ± STD, n= 7472), which is much shorter than the spindle length which is approximately 5 µm (Table 1, Suppl. Fig. 1B). Likewise, in anaphase, the average length of microtubules is 0.58 µm ± 0.52 µm (STD, n=7011, early anaphase), 0.62 µm ± 0.49 µm (STD, n=3317, mid anaphase) and 0.59 µm ± 0.45 µm (STD, n=1212, late anaphase), see (Table 1, Suppl. Fig. 1B), which is much shorter than the spindle (3-4 µm). Furthermore, we determined the position of the pole-proximal ends of microtubules along the spindle axis. In metaphase, these putative microtubule minus-ends were found throughout the spindle (Fig. 1C, Suppl. Fig. 1D), with no marked preference for the poles. In anaphase, about 40% of microtubule ends are found within a distance of

500 nm from the chromosomes, and the others are distributed throughout the spindle (Fig. 1D, Suppl. Fig. 1E).

Together, these findings confirm that the acentrosomal female meiotic spindle is an array of short microtubules, more similar to meiotic Xenopus spindles than to mitotic spindles in *C. elegans,* as previously suggested by others (Srayko et al 2006, Brugués et al 2012). We conclude that the distance between poles in metaphase (5 µm) and chromosomes in anaphase (3-4 µm) is bridged by an array of short overlapping microtubules rather than long ones spanning the entire distance.

Meiotic spindles are composed of short-lived, fast moving microtubules

We next sought to understand the role of microtubule movements and dynamics in the structural changes observed during the transition from metaphase to anaphase. Since electron tomography generates static snapshots, we investigated this question by light microscopy.

Using Fluorescence Recovery After Photo bleaching (FRAP), we first measured microtubule turnover and motion in metaphase I spindles. By photobleaching a small stripe near the center as well as close to the poles of metaphase spindles (Fig. 2A, arrows, Suppl. Movie 4), we observed a half-time of microtubule recovery in metaphase of 4.9 s ± 3.4 s (n=6) in the spindle center and 4.1 s ± 2.7 s (n=6) at the spindle poles (Fig. 2B). In addition, we observed that the photo-bleached stripes close to the spindle poles showed a rapid poleward movement with a rate of 8.5 ± 2.2 µm/min (n=6, Fig.2C).

We conclude that microtubules in *C. elegans* meiosis turn over rapidly and show substantial poleward motion. This is notably different from the first mitotic division in the early *C. elegans* embryos, where microtubule motion was not detected in similar experiments (Labbe et al., 2004; Redemann et al., 2017). Thus, in female meiosis, both nucleation/depolymerization and microtubule motion might be involved in shaping the spindle structure.

Spindle rearrangements during meiosis correlate with substantial changes in microtubule number.

To better understand the role of microtubule polymerization dynamics, we next asked whether the number of spindle microtubules changed during spindle rearrangements. From our reconstructions (Table 1, Suppl. Fig. 1B) we detected 3662 and 3812 microtubules in metaphase, 7011 microtubules in early anaphase (Table 1, Suppl. Fig. 1B), 3317 in mid anaphase and 1511 and 1306 microtubules in late anaphase. To get a more spatially resolved picture, we also measured the number of microtubules along the spindle axis in our datasets. This measurement showed that the number of microtubules increases by more than 2-fold in the center of the spindle from metaphase to early anaphase, while the number of microtubules decreases from the spindle poles. Throughout anaphase the number of microtubules then decreased slightly on the poles and almost halved in the spindle center (Fig. 3A-D). Thus, we conclude that changing the number of microtubules is an important part of the structural spindle rearrangements that occur during meiosis.

Microtubule rearrangements during meiosis are driven by changes in microtubule dynamics, not nucleation rates alone.

We next sought to gain insight into the mechanisms that drive the observed changes in microtubule numbers. We first asked whether changes in nucleation rate alone could explain the data. If this were the case, microtubule growth, shrinkage, and severing rates would remain the same, and the average length of the microtubules would remain unchanged throughout meiosis. However, the net polymer amount would change in step with microtubule number.

Interestingly, we found the opposite result, whereby the net polymer amount of microtubules remained almost constant from metaphase to anaphase even though the number of microtubules increases 2-fold. Furthermore, during the same time, the average length of microtubules went down by a factor of 2 (Fig. 1B, Suppl. Fig. 1C, Table 1). Only in late anaphase, as the spindle continued to elongate, did the number of microtubules and the net polymer length start to decrease. Therefore, the observed changes in spindle morphology were not caused by changes in nucleation rates alone, but also by changes in microtubule disassembly. In principle this could be caused by local or global changes in microtubule severing, changes in microtubule growth dynamics, or a combination thereof. In the following, we will try to disentangle these possibilities.

Microtubule dynamics during spindle rearrangement are globally regulated

We next investigated whether changes in microtubule length were uniform along the spindle axis (Fig. 4A-D). This analysis revealed that, during the transition from metaphase to early anaphase, the average length of microtubules decreased everywhere in the spindle simultaneously. Both in metaphase (Fig. 4E, I, Suppl. Fig. 2) and in anaphase (Fig. 4F-H, J-L Suppl. Fig. 2), the fraction of short microtubules was higher near the spindle poles, which in anaphase is located at the inner surface of the chromosomes. Throughout anaphase, the most noticeable spatial asymmetry was that there are fewer microtubules in the spindle half closer to the cell cortex and that those microtubules were somewhat shorter than those facing the cytoplasm (Fig. 3, Fig. 4B, C). This difference was most apparent in early and mid anaphase, with 1.17μm ± 0.8 vs 1.00μm ± 0.6 ($p = 3.6$ E-6) in early anaphase and 1.04 μm ± 0.6 vs 0.91 ± 0.53 ($p = 0.002$). Together, our data suggest that while there is some intrinsic asymmetry in the spindles, the changes in microtubule dynamics that characterize spindle rearrangements are likely regulated globally, without much spatial fine tuning.

A mathematical model for microtubule dynamics reveals the relative importance of microtubule severing and growth dynamics

We next sought to better understand the processes that drive the observed microtubule length changes during spindle rearrangements. For this we constructed a mathematical model that solves for the expected microtubule length distribution given their growth velocity v_g, their rate of undergoing catastrophe r and the rate at which microtubules are cut per unit time and length κ. The stability of microtubule plus ends created by cutting,

is encoded in the parameter α, which interpolates between the two extreme cases ($\alpha = 0$), where newly created plus ends immediately depolymerize and ($\alpha = 1$) where newly created plus ends are indistinguishable from preexisting ones (see Fig. 5). The mathematical details of this model are given in the appendix (Suppl. Material 1). In spirit, it is very similar to the model proposed in (Kuo et al 2019).

We used this mathematical model to infer the relative importance of microtubule cutting and changes in microtubule nucleation. Using Markov Chain Monte Carlo sampling (Foreman-Mackey et al 2013, MacKay & MacKay 2003), we infer the most likely values for the dimensionless ratios $\bar{r} = r/v_g\ell$, and $\bar{\kappa} = \kappa/v_g\ell^2$, where ℓ is the average microtubule length given the experimentally determined microtubule length distribution, see Appendix (Suppl. Material 1). Importantly this inference scheme only uses the experimentally measured microtubule length distribution as input, and allows us to quantify the relative importance of cutting to turnover $\bar{r}/\bar{\kappa}$ independently of direct measurements of turnover rates and microtubule growth velocities, which are hard to do in these very small spindles. In Figure 6 we show the inferred posterior probabilities of model parameters based on the data (Fig. 6A-D). We then compared the predictions of the model parameterized by the expectation values of all parameters to our data (Fig. 6E-H).

We first asked whether the transition of spindle structure from metaphase to early anaphase can be explained by microtubule turnover, which here means changes in growth rate and catastrophe, or microtubule cutting. We report our results in terms of the non-dimensionalized turnover rate $\bar{r} = r/v_g\ell$, and the non-dimensionalized cutting rate

$\bar{\kappa} = \kappa/v_g\ell^2$, where ℓ is the average microtubule length. Most importantly the ratio of these two quantities $\bar{r}/\bar{\kappa}$ gives the length (in units of average MT length) a microtubule has to reach for it to be more likely to get severed than to undergo catastrophe. This quantifies the relative importance of turnover to cutting; for example, if $\bar{r}/\bar{\kappa}$ is much smaller then 1 this indicates a length distribution that is dominated by cutting, if $\bar{r}/\bar{\kappa}$ is much larger than 1, it indicates a length distribution that is dominated by catastrophe and turnover. In metaphase (Fig 6A, B, E, F) and early anaphase (Fig. 6C, G) we find that the non-dimensionalized turnover rate $\bar{r} = r/v_g\ell$ is equal to 1.0, while the non-dimensionalized cutting rate $\bar{\kappa} = \kappa/v_g\ell^2$ is about 0.1. Here, ℓ is the average microtubule length. These numbers imply that the length at which a microtubule is more likely to be cut than to undergo catastrophe is $\bar{r}/\bar{\kappa} \simeq 10$, *i.e.,* cutting is a relatively rare event. In fact, there are no microtubules in metaphase that are longer than 10 times the average microtubule length $\ell = 1\mu\mathrm{m}$ (*i.e.,* 10 μm) and only 1 microtubule was larger than *10 times the average length* $\ell = 0.5\mu\mathrm{m}$ (*i.e.,* 5 μm) in early anaphase. This also implies that the change in the microtubule length observed from metaphase (ℓ = 1 μm) to early anaphase (ℓ = 0.5 micron), is a consequence of either the microtubule turnover rate, or changes in microtubule growth velocity.

We next use our estimate for the ratio $\bar{r} = r/v_g\ell$ to infer the microtubule growth velocity in meiotic metaphase spindles. For this we take the measured FRAP half-life in metaphase (see Fig 2B) of about 5s as an estimate for microtubule turnover time 1/r and determine the average microtubule length of about 1 μm (Table 1). Using these values, we estimate that the microtubule growth velocity (vg) during metaphase is close to 12 μm/min.

Interestingly, this agrees with growth velocity estimates based on microtubule flux, and it is similar to values reported for microtubule growth rates in the dense regions of mitotic *C. elegans* spindles (Redeman et al 2017). Notably, this value is slower than growth rates reported for astral microtubules growing away from centrosomes reported by (Redeman et al 2017, Srayko et al 2005). This suggests that microtubule growth velocities are under spatial and temporal control within the cytoplasm, as was previously described by (Geisterfer et al 2019, Walczak et al 2016)

The drastic change in the average microtubule length from metaphase to anaphase could be due to a decrease in microtubule growth velocity to half its metaphase value (6 μm/min). Alternatively, it could also be caused by an increase in microtubule turnover rate. Given the large relative errors of the FRAP measurements in the very small meiotic spindles, we cannot definitely answer whether microtubule growth speed, turnover rate, or both are under biochemical control at this stage. In toto, our data argue that the transition from metaphase to early anaphase is best explained by modulating microtubule growth and polymerization dynamics, and not by increased microtubule cutting. Note that a role for katanin in amplification of microtubule mass and number has been suggested *in vitro,* where severing activity can result in the incorporation of GTP-tubulin into the microtubule lattice, thus increasing the rescue frequency and stability of newly emerging microtubule ends (Vemu et al 2018).

We finally asked the same question for the transition from early to mid anaphase. We find that later in anaphase the relative importance of cutting increases with $\bar{\kappa}$ = 0.3, and $\bar{r}$ = 0.9, see Fig 6D, H. This means that at this later point, the length at which a microtubule

is more likely to be cut than to undergo catastrophe comes down to 3 ℓ, which would be approximately 3% of the microtubule population.

Thus, our data suggest that the initial steps of the transition from metaphase to anaphase are due to changes in microtubule turnover rate and growth and not mediated by katanin dependent severing. This is surprising since earlier work clearly demonstrated the importance of severing during spindle assembly (Srayko et al 2006, McNally et al 2011, McNally et al 2014, Connolly et al 2014, Joly et al 2016). Estimates of the number of Katanin mediated cutting events by counting lateral defects in partial EM reconstructions of meiotic spindles at earlier stages had found a large number of cutting events in wildtype spindles (Srayko et al 2006). To test the predictions of our inference scheme we decided to look for similar cutting sites in our datasets.

Analysing the frequency of lateral defects in our tomographic data, indicated a very low abundance (1.1% of microtubules in Metaphase #2, 2.5% in early anaphase and 1.8% in mid Anaphase). We could also not detect an increased occurrence of lateral defects in longer microtubules or at distinct positions within the spindle. This is notably less than what was reported for earlier spindles. We conclude that the initial steps of the transition from metaphase to anaphase are due to changes in microtubule turnover rate and growth and not mediated by katanin dependent severing.

Discussion

Acentrosomal meiotic spindles in *C. elegans* undergo a reorganization from a bipolar microtubule arrangement in metaphase to an inter-chromosomal microtubule array in

anaphase. Along with this microtubule reorganization, chromosomes are segregated to extrude half of the genetic material as polar bodies. The underlying mechanism of the microtubule reorganization is not very well understood, and several mechanisms could be involved, for instance katanin mediated severing (Joly et al 2016, Srayko et al 2006), transport of microtubules (Mullen & Wignall 2017, Brugués et al 2012) or changes in microtubule polymerization dynamics (Brugués et al 2012, Needleman et al 2010). Here we have generated complete 3D reconstructions of meiotic spindles in *C. elegans* at different stages and combined this ultrastructural analysis with light microscopy and simulations to investigate the rearrangement of microtubules during meiosis.

Based on light microscopy, previous publications suggested that the microtubule rearrangement from metaphase to anaphase in meiosis could be driven by an initial inward sliding of antiparallel microtubules by kinesin 14 family members (McNally 2016) and a subsequent depolymerization of microtubules at the spindle pole, due to severing by katanin (McNally 2006). This was based on the observation that the initial phase of spindle shortening is accompanied by an increase of microtubule density, followed by a further shortening and depolymerization of microtubules at the spindle poles, resulting in a decrease of microtubule density. In agreement with this, our tomographic reconstructions show an initial increase in microtubule number and density during early anaphase, which is followed by a decrease in microtubule number and density in mid anaphase. However, while inward sliding of microtubules would result in an increased density, it does not explain the observed 2-fold increase of microtubule number. In addition, our data showed a poleward directed movement of microtubules, contradicting

an inward sliding. This suggests that inward sliding is unlikely to contribute to spindle shortening and cannot account for the appearance of microtubules between the chromosomes that characterizes anaphase.

The reorganization of microtubules could alternatively be driven by a selective depolymerization of microtubules at the spindle poles. However, our data suggests that the spindle rearrangement is mainly driven by global changes in microtubule nucleation and turn-over. A more local analysis of the changes in microtubule length and number, which isolates pole proximal from pole distal microtubules, (Fig. 3 and 4) as well as investigations of local changes using the mathematical model (Supp. Fig. 3) showed no spatial differences in microtubule properties and dynamics.

Our data showed that spindles are made from arrays of dynamic short microtubules, that turnover within 5 seconds. We further showed that the dramatic structural rearrangements observed from metaphase to anaphase are correlated with drastic changes in the microtubule number and length distribution. Meiotic metaphase spindles are composed of fewer but longer microtubules, while spindles in early anaphase are made of more but shorter microtubules.

These observations led us to ask whether severing of microtubules by katanin, or an increase in microtubule dynamics, allowing more nucleation and/or higher rates of catastrophe, would better explain our observations. For this we developed a mathematical model that predicts the microtubule length distribution from cutting rates and turnover dynamics. We inferred parameters for the model using the microtubule length distribution and numbers found in electron tomography. This analysis severely constrains

the possible mechanisms for spindle restructuring from metaphase to anaphase. While Katanin is clearly important for spindle assembly (Srayko et al 2006, McNally et al 2011, McNally et al 2014, Connolly et al 2014, Joly et al 2016) our data suggest that cutting is of relatively minor importance for the transition from metaphase to at least until mid anaphase. The early phases of spindle rearrangement are likely driven by changes in microtubule nucleation, growth and turnover.

Interestingly, a role for microtubule severing proteins, including katanin, in microtubule amplification has recently been suggested. Here, katanin induces nanoscale damage to the microtubule lattice, resulting in the incorporation of GTP tubulin (Vemu et al 2018, Schaedel et al 2015, 2019) and stabilization of microtubules. The incorporation of GTP into the lattice is thought to have two effects: promoting rescue as well as the stability of a new plus-end formed upon severing. This would result in an amplification of microtubules. Consistent with this, our data shows a two-fold increase of microtubule number during the transition from metaphase to early anaphase. Similarly, Srayko *et al* 2006 reported a decrease in microtubule number in *C. elegans* embryos depleted of katanin. However, analysing the frequency of lateral defects in our tomographic data, which presumably represents the action of katanin, indicated a very low abundance (1.1% of microtubules in Metaphase #2, 2.5% in early anaphase and 1.8% in mid Anaphase). We could also not detect an increased occurrence of lateral defects in longer microtubules or at distinct positions within the spindle. Based on in vitro data, it also seems that the timescale of severing by katanin, which is in the range of 10ths of seconds, might exceed

the actual lifetime of microtubules within the spindle, which is approximately 5s. This data directly supports the prediction of the mathematical model that microtubule severing is a rare event during the transition from metaphase to anaphase and is thus not the main contributor for spindle reorganization.

In summary, by combining light microscopy with electron tomography and mathematical modeling we analyzed the reorganization of microtubules during the transition from metaphase to anaphase in *C. elegans* meiotic embryos. Our data suggests that this reorganization is driven by temporal global changes in microtubule growth and/or turn-over.

Acknowledgements

The authors are thankful to Th. Müller-Reichert for continuous support and to S. Tulok and Dr. A. Walther (Core Facility Cellular Imaging, Faculty of Medicine Carl Gustav Carus, TU Dresden) for help with light microscopy. The authors are also grateful to the members of the electron and light microscopy facility at the Max Planck Institute of Molecular Cell Biology and Genetics (MPI-CBG, Dresden) for technical assistance and J.

Baumgart (MPI-PKS, Dresden) for initial help in data analysis. The authors would like to thank Drs. E. O'Toole and R. McIntosh (Boulder) for a critical reading of the manuscript. Ina Lantzsch and Erik Szentgyörgyi were supported by funds from the Deutsche Forschungsgemeinschaft (MU 1423/3-1, 3-2 and 8-1 to T. Müller-Reichert) and the Human Frontier Science Programme (RGP 0034/2010 to D. N. and T.M.R). S. Redemann received funding from the Faculty of Medicine Carl Gustav Carus of the TU Dresden (Frauenhabilitationsstipendium).

Materials and methods

Worm strains and gene silencing by RNAi

Worm strains

The following *C. elegans* strains were used in this study: strain MAS91 (unc-119(ed3) III; ItIs37[pAA64; pie-1::mCherry::HIS58]; ruIs57[pie-1::GFP::tubulin + unc-119(+)]) for live-cell imaging and correlative light microscopy/electron tomography, strain SA250 (tjIs54 [pie-1p::GFP::tbb-2 + pie-1p::2xmCherry::tbg-1 + unc-119(+)]; tjIs57 [pie-1p::mCherry::his-48 + unc-119(+)]) for FRAP experiments. Strains were cultured and maintained at 16°C as described (Brenner, 1974).

Light microscopy

Sample preparation for light microscopy

Oocytes for live-cell imaging were prepared as described previously (Woog et al., 2012). For FRAP measurements, meiotic spindles in oocytes were observed in the uterus of adult hermaphrodites (strain SA250) mounted on a thin 4% Agarose pad between a slide and a coverslip. Polystyrene microspheres (Microspheres 0.10 μm, Polysciences, Inc.) were added to the agar solution before specimen mounting to immobilize the living worms.

Spinning disk confocal fluorescence imaging

Live imaging was performed using a spinning disk confocal microscope (Nikon Ti2000, Yokugawa CSU-X1), equipped with 488-nm and 561-nm diode lasers, an EMCCD camera (Hamamatsu), and a 60X water-immersion objective (CFI Plan Apo VC 60X WI, NA 1.2,

Nikon). Acquisition parameters were controlled using a home-developed LabVIEW program (LabVIEW, National Instruments). Images were acquired every 1 second with a single z-plane.

FRAP experiments

The photobleaching system was constructed on the above-mentioned spinning disk confocal microscope. 80-MHz femtosecond pulsed laser with 0.3-nJ pulse energy and 800-nm center wavelength was used for performing photobleaching and generated from a Ti:sapphire pulsed laser (Mai-Tai, Spectra-Physics, Mountain View, CA). The photobleaching laser was focused through the same objective for imaging, and photobleaching was performed by moving the sample on a piezo-stage (P-545 PIano XYZ, Physik Instrumente) in three dimensions controlled by a home-developed LabVIEW program (LabVIEW, National Instruments). Scanning line-bleaching with z-steps were created by moving the stage perpendicular to the pole-to-pole axis back and forth on the focal plane while lowering the stage in the z direction. The parameter for bleaching in length by depth was 6 x 2 μm. The moving speed of the stage was 50 μm/sec.

Analysis of fluorescence recovery after photobleaching and microtubule poleward flux

Fluorescence recovery after photobleaching (FRAP) and rate of microtubule poleward flux was calculated with a combination of Fiji (Schindelin et al., 2012) and Matlab (MATLAB and Statistics Toolbox Release 2012, The MathWorks, Nitick, USA). Time-lapse images of spindles expressing GFP::tubulin and mCherry::histone (corresponding to

chromosomes) were realigned in a routine for matching, rotation and translation using Rigid Body of Fiji's StackReg plug-in, so that the random displacement of the spindle due to the spontaneous motion of the worm was corrected.

Poleward flux and recovery of photobleached makers were tracked using a program written in Matlab (MATLAB and Statistics Toolbox Release 2012, The MathWorks, Nitick, USA). Line-scans of GFP-labeled tubulin along the metaphase spindle were extracted over the course of anaphase. To track the microtubule poleward flux, each line-scan at each time point can be divided into two halves by the middle plane of the spindle. The half of the line profile with the bleached mark was subtracted from the other half of the non-bleached profile by a reflection of symmetry around the middle plane of the spindle. This profile subtraction was used to remove spatial variations in the background fluorescence, a valid procedure assuming mirror symmetry of the spindle around its middle plane. A Gaussian function was used to fit the subtracted profile to locate the center of the bleached mark, and thus the position of the bleached mark versus time was extracted. A straight line was fitted to the position of the bleached mark versus time to retrieve the rate of the bleached mark. The recovery time of GFP::tubulin after photobleaching was determined by using an exponential fit. The fluorescence intensities of photobleached marks were calculated by summing intensities over 3 pixels (~0.5 μm) around the center of the photobleach mark.

Electron microscopy

Sample preparation

Samples for electron tomography were prepared as described (Woog et al., 2012). Briefly, hermaphrodites were dissected in Minimal Edgar´s Growth Medium (Edgar, 1995) and embryos in early meiosis were selected and transferred to cellulose capillary tubes (Leica Microsystems, Vienna, Austria) with an inner diameter of 200 µm. The embryos were observed with a stereomicroscope, transferred to membrane carriers at appropriate stages and immediately cryo-immobilized using an EMPACT2 high-pressure freezer (Leica Microsystems, Vienna, Austria) equipped with a rapid transfer system (Pelletier et al., 2006). Freeze substitution was performed over 3 d at -90°C in anhydrous acetone containing 1% OsO_4 and 0.1% uranyl acetate using an automatic freeze substitution machine (EM AFS, Leica Microsystems, Vienna, Austria). Epon/Araldite infiltrated samples were then embedded in a thin layer of resin and polymerized for 3 d at 60°C. Embedded embryos were re-mounted on dummy blocks and serial semi-thick (300 nm) sections were cut using an Ultracut UCT Microtome (Leica Microsystems, Vienna, Austria). Sections were collected on Formvar-coated copper slot grids and post-stained with 2% uranyl acetate in 70% methanol followed by Reynold's lead citrate.

Electron tomography

For dual-axis electron tomography (Mastronarde et al 1997), 15-nm colloidal gold particles (Sigma-Aldrich) were attached to both sides of semi-thick sections to serve as fiducial markers for subsequent image alignment. Series of tilted views were recorded using a TECNAI F30 transmission electron microscope (FEI Company, Eindhoven, The

Netherlands) operated at 300 kV. Images were captured every 1.0° over a ± 60° range at a pixel size of 2.3 nm using a Gatan US1000 2K x 2K CCD camera. Using the IMOD software package, a montage of 2 x 1 [meiosis I: metaphase #1, metaphase #2, anaphase (late) #1, anaphase (late) #2; meiosis II: metaphase #1, metaphase #2] or 2 x 2 [meiosis I: anaphase (early); meiosis II: anaphase (late)] frames was collected and combined for each serial section to cover the lengths of the meiotic spindles (Kremer et al., 1996; Mastronarde, 1997).

For image processing the tilted views were aligned using the positions of the fiducials. Tomograms were computed for each tilt axis using the R-weighted back-projection algorithm (Gilbert, 1972). In order to cover the entire volume of each spindle, we acquired tomograms of about 8-12 consecutive sections per sample. In total, we recorded 10 wild-type spindles in meiosis I and II (Supplementary Table 1 and 2).

Three-dimensional reconstruction and automatic segmentation of microtubules

We used the IMOD software package (http://bio3d.colorado.edu/imod) for the calculation of electron tomograms (Kremer et al., 1996). We applied the Amira software package for the segmentation and automatic tracing of microtubules (Stalling et al., 2005). For this, we used an extension to the filament editor of the Amira visualization and data analysis software (Redemann et al., 2017; Redemann et al., 2014; Weber et al., 2012). We also used the Amira software to stitch the obtained 3D models in *z* to create full volumes of the recorded spindles (Redemann et al., 2017; Weber et al., 2014). The

automatic segmentation of the spindle microtubules was followed by a visual inspection of the traced microtubules within the tomograms. Correction of the individual microtubule tracings included: manual tracing of undetected microtubules, connection of microtubules from section to section and deletions of tracing artifacts (e.g. membranes of vesicles). Approximately 5% of microtubules needed to be corrected (Redemann et al., 2017).

Data and error analysis

Data analysis was performed using either the Amira software package or by exporting the geometric data of the traced microtubules followed by an analysis using MatLab (MATLAB and Statistics Toolbox Release 2012, The MathWorks, Nitick, USA). In our analysis of spindle structure, the following errors were considered (Redemann et al., 2017). Briefly, during the data preparation and the imaging process, the tomograms are locally distorted. Furthermore, the exposure of the electron beam causes a shrinking of the sample. During the reconstruction of the microtubules, however, the most important errors occur in the tracing and matching process. In addition, the data is again distorted in all directions to align the tomograms. We assumed that this distortion primarily compensates the distortion of the imaging process. For the tracing, the error was previously analyzed for reconstructions of *C. elegans* centrosomes (Weber et al., 2012). We assumed that the error lies in the same range of 5-10%. In addition, the traced microtubules were manually verified. It is more difficult to estimate the error of the matching algorithm (Weber et al., 2014), since it depends on the local density and properties of the microtubules. The quality of our analysis should be influenced only by minor 3D distortions.

Quantification of tomographic data

Microtubule length and positioning

The reconstruction algorithm for microtubules in serial-section electron microscopy represents each microtubule as a 3D piecewise linear curve $(p_1, \dots, p_n)$, $p_i \in R^3$, of its

centerline. Thus, the length of the microtubule is given by the sum of the lengths of the line segments $\sum_{i=1}^{n-1} \|p_i - p_{i+1}\|$.

Figure legends

Figure 1. Three-dimensional organization of microtubules

A, Three-dimensional models showing full reconstruction of microtubules at different stages of wild-type meiosis I. The different stages from metaphase to late anaphase are indicated. Microtubules are shown in green, chromosomes in grey. An individual color is assigned to each data set. The anaphase datasets are oriented with the cortical side being left, cytoplasmic right. **B**, Length distribution of microtubules at specific meiotic stages. Data sets are represented by their assigned colors (insert). **C**, Cumulative distance function of the pole-proximal microtubule endpoints in metaphase. The position of the spindle poles in the schematic drawing and the data sets is indicated (stars). **D**, Cumulative distance function of the chromosome-proximal microtubule endpoints in anaphase. The position of the poles is indicated (stars).

Figure 2. Microtubule dynamics during metaphase of meiosis I

A, Light microscope images of spindles in meiosis I prior to and after photo bleaching at the spindle center (top row, red arrows) and close to the spindle pole (bottom row, green arrows). The bleaching of the sample (t=0) and the frame rate are indicated. **B**, Plot of the recovery of the bleach mark over time at the center (magenta, mean values given in blue) and pole (green, mean values given in black) for different datasets. The recovery times for

the data sets are shown in the plot. **C**, Plot showing the poleward motion of the bleach mark at the spindle pole over time for different datasets (blue). The mean is indicated in black.

Figure 3. Analysis of microtubule number along the spindle axis

A-D, Plots of the number of microtubules at different positions (100 nm steps) along the spindle axis for four different datasets in metaphase #2, early anaphase, mid and late anaphase #1. The approximate position of chromosomes is indicated by grey outlines. The datasets are oriented with '0' being at the cortical side.

Figure 4. Detailed analysis of microtubule length along the spindle axis

A-D, Plots of the average microtubule length at different positions (100nm steps) along the spindle axis for four different datasets in metaphase #2, early anaphase, mid and late anaphase #1. Shaded color indicates the standard deviation, datasets are oriented with '0' being at the cortical side. **E-H**, Tomographic reconstructions of microtubules of 500nm and shorter for the datasets shown in A-D **I-L**, Plots showing the number of microtubules, which are 500nm and shorter along the spindle axis for the datasets shown above. The approximate position of chromosomes is indicated by grey outlines.

Figure 5. Processes determining microtubule length distributions

Our model considers microtubule turnover with a rate r, and cutting with a rate kappa. Alpha is the stability of cutting generated MT plus-ends.

Figure 6. Simulation of possible mechanisms for microtubule rearrangement

A, Likelihood distribution of model parameters determined by Markov Chain Monte-Carlo for Metaphase #1. The top boxes show the totally marginalized distribution of parameters, with dashed lines delimiting the 95% confidence interval. Surface plots show cuts through the likelihood distributions, marginalized onto 2D subspaces. Lines are contour lines, dots indicate MCMC-samples. **B**, Same as in A but for the Metaphase #2 dataset. **C**, Same as in A but for the Anaphase (early) dataset. **D**, Same as in A but for the Anaphase (mid) dataset. **E, F, G, H** Comparison of experimentally determined length distribution of microtubules (dots) to the prediction of the highest likelihood model (solid line) for Metaphase #1 (**E**), Metaphase #2 (**F**), Anaphase (early) (**G**) and Anaphase (mid) (**H**).

Table

Table 1. Summary of quantifications of tomographic data for meiosis I

The spindle length, the total number of microtubules, the average microtubule length, the maximum length of microtubules and the total length of all microtubules in the spindle is shown for each tomographic data set.

Supplementary figures

Suppl. Figure 1. Three-dimensional organization of microtubules in meiosis II

A, Three-dimensional models showing full reconstructions of microtubules at different stages of wild-type meiosis. The different stages from metaphase to late anaphase are indicated. Microtubules are shown in green, chromosomes in grey. **B**, Quantitative analysis of microtubule organization corresponding to the meiotic stages as shown in **A**. An individual color is assigned to each data set. **C**, Length distribution of microtubules at specific meiotic stages. Data sets are represented by their assigned colors (insert). **D**, Cumulative distance function of the pole-proximal microtubule endpoints in metaphase. **E**, Cumulative distance function of the chromosome-proximal microtubule endpoints in anaphase.

Suppl Figure 2. Detailed analysis of microtubule length along the spindle axis in meiosis II

A-C, Plot of the average microtubule length at different positions (100nm steps) along the spindle axis for three different datasets in metaphase #2, early anaphase, and mid anaphase #1. Standard deviation is indicated by the shaded areas **D-F**, Plots showing the number of microtubules, which are 500nm and shorter along the spindle axis for the datasets shown above. **G-I**, Plot showing the number of microtubules along the spindle axis for metaphase #2, early anaphase, and mid anaphase in meiosis II.

Suppl Figure 3. Simulation of possible local mechanisms for microtubule rearrangement

A, Likelihood distribution of model parameters determined by Markov Chain Monte-Carlo for poleward Microtubules (center of MT is located near the poles) in Metaphase #1. The top boxes show the totally marginalized distribution of parameters, with dashed lines delimiting the 95% confidence interval. Surface plots show cuts through the likelihood distributions, marginalized onto 2d subspaces. Lines are contour lines, dots indicate MCMC-samples. **B**, Same as in A but for the Metaphase #2 dataset. **C**, Comparison of experimentally determined length distribution of microtubules (dots) to the prediction of the highest likelihood model (solid line) for Metaphase #1 (**C**), and Metaphase #2 (**D**.

Supplementary movies

Suppl. Movie 1. Visualization of spindle ultrastructure in meiosis I at mid anaphase

This movie (corresponding to Figure 1A; anaphase, mid) shows a close up-view of the microtubules organization at mid anaphase. Microtubules are visualized in green, chromosomes in grey.

Suppl. Movie 2. Visualization of spindle ultrastructure in meiosis I at late anaphase

This movie (corresponding to Figure 1A; anaphase, late #1) shows a close up-view of the microtubules organization at late anaphase. Microtubules are visualized in green, chromosomes in grey.

Suppl. Movie 3. Visualization of spindle ultrastructure in meiosis I at late anaphase

This movie (corresponding to Figure 3A; anaphase, late #2) shows a close up-view of the microtubules organization at late anaphase. Microtubules are visualized in green, chromosomes in grey.

Suppl. Movie 4. FRAP during metaphase in Meiosis I

Movie of a FRAP experiment during metaphase in meiosis I of *C. elegans* expressing GFP tubulin and mCherry Histone. A small stripe is bleached next to the Chromosomes (right side) and the motion and recovery of the stripe over time are analyzed. Framerate 1fps.

1

References

Albertson, D. G., & Thomson, J. N. (1993). Segregation of holocentric chromosomes at meiosis in the nematode, Caenorhabditis elegans. *Chromosome Research*, *1*(1), 15-26.

Brenner, S. (1974). The genetics of Caenorhabditis elegans. *Genetics*, *77*(1), 71-94.

Brugués, J., Nuzzo, V., Mazur, E., & Needleman, D. J. (2012). Nucleation and transport organize microtubules in metaphase spindles. *Cell*, *149*(3), 554-564.

Connolly, A. A., Osterberg, V., Christensen, S., Price, M., Lu, C., Chicas-Cruz, K., ... & Bowerman, B. (2014). Caenorhabditis elegans oocyte meiotic spindle pole assembly requires microtubule severing and the calponin homology domain protein ASPM-1. *Molecular biology of the cell*, *25*(8), 1298-1311.

Dumont, J., Oegema, K., & Desai, A. (2010). A kinetochore-independent mechanism drives anaphase chromosome separation during acentrosomal meiosis. *Nature cell biology*, *12*(9), 894-901.

Edgar, L. G. (1995). Blastomere culture and analysis. In *Methods in cell biology* (Vol. 48, pp. 303-321). Academic Press.

Fabig, G., Kiewisz, R., Lindow, N., Powers, J. A., Cota, V., Mateo, L. J., ... & Müller-Reichert, T. (2020). eLife 2020;9:e50988 DOI: 10.7554/eLife.50988

Foreman-Mackey, D., Hogg, D. W., Lang, D., & Goodman, J. (2013). emcee: the MCMC hammer. *Publications of the Astronomical Society of the Pacific*, *125*(925), 306.

Geisterfer, Z. M., Zhu, D. Y., Mitchison, T., Oakey, J., & Gatlin, J. C. (2019). Microtubule growth rates are sensitive to global and local changes in microtubule plus-end density. *bioRxiv*, 849190.

Gilbert, P. F. C. (1972). The reconstruction of three-dimensional structure from projections and its application to electron microscopy II. Direct methods. *Proceedings of the Royal Society of London. Series B. Biological Sciences*, *182*(1066), 89-102.

Hassold, T., & Hunt, P. (2001). To err (meiotically) is human: the genesis of human aneuploidy. *Nature Reviews Genetics*, *2*(4), 280-291.

Holubcová, Z., Blayney, M., Elder, K., & Schuh, M. (2015). Error-prone chromosome-mediated spindle assembly favors chromosome segregation defects in human oocytes. *Science*, *348*(6239), 1143-1147.

Joly, N., Martino, L., Gigant, E., Dumont, J., & Pintard, L. (2016). Microtubule-severing activity of the AAA+ ATPase Katanin is essential for female meiotic spindle assembly. *Development*, *143*(19), 3604-3614.

Kremer, J. R., Mastronarde, D. N., & McIntosh, J. R. (1996). Computer visualization of three-dimensional image data using IMOD. *Journal of structural biology*, *116*(1), 71-76.

Kuo, Y. W., Trottier, O., Mahamdeh, M., & Howard, J. (2020). Effects of Severing Enzymes on the Length Distribution and Total Mass of Microtubules. *Biophysical Journal*, *118*(3), 598a.

Laband, K., Le Borgne, R., Edwards, F., Stefanutti, M., Canman, J. C., Verbavatz, J. M., & Dumont, J. (2017). Chromosome segregation occurs by microtubule pushing in oocytes. *Nature communications*, *8*(1), 1-11.

Labbé, J. C., McCarthy, E. K., & Goldstein, B. (2004). The forces that position a mitotic spindle asymmetrically are tethered until after the time of spindle assembly. *The Journal of cell biology*, *167*(2), 245-256.

MacKay, D. J., & Mac Kay, D. J. (2003). *Information theory, inference and learning algorithms*. Cambridge university press.

Mastronarde, D. N. (1997). Dual-axis tomography: an approach with alignment methods that preserve resolution. *Journal of structural biology*, *120*(3), 343-352.

McNally, K., Audhya, A., Oegema, K., & McNally, F. J. (2006). Katanin controls mitotic and meiotic spindle length. *The Journal of cell biology*, *175*(6), 881-891.

McNally, K. P., & McNally, F. J. (2011). The spindle assembly function of Caenorhabditis elegans katanin does not require microtubule-severing activity. *Molecular biology of the cell*, *22*(9), 1550-1560.

McNally, K., Berg, E., Cortes, D. B., Hernandez, V., Mains, P. E., & McNally, F. J. (2014). Katanin maintains meiotic metaphase chromosome alignment and spindle structure in vivo and has multiple effects on microtubules in vitro. *Molecular biology of the cell*, *25*(7), 1037-1049.

McNally, K. P., Panzica, M. T., Kim, T., Cortes, D. B., & McNally, F. J. (2016). A novel chromosome segregation mechanism during female meiosis. *Molecular biology of the cell*, *27*(16), 2576-2589.

Mullen, T. J., & Wignall, S. M. (2017). Interplay between microtubule bundling and sorting factors ensures acentriolar spindle stability during C. elegans oocyte meiosis. *PLoS genetics*, *13*(9), e1006986.

Needleman, D. J., Groen, A., Ohi, R., Maresca, T., Mirny, L., & Mitchison, T. (2010). Fast microtubule dynamics in meiotic spindles measured by single molecule imaging: evidence that the spindle environment does not stabilize microtubules. *Molecular biology of the cell*, *21*(2), 323-333.

Pelletier, L., O'Toole, E., Schwager, A., Hyman, A. A., & Müller-Reichert, T. (2006). Centriole assembly in Caenorhabditis elegans. *Nature*, *444*(7119), 619-623.

Redemann, S., Weber, B., Möller, M., Verbavatz, J. M., Hyman, A. A., Baum, D., ... & Müller-Reichert, T. (2014). The segmentation of microtubules in electron tomograms using Amira. In *Mitosis* (pp. 261-278). Humana Press, New York, NY.

Redemann, S., Baumgart, J., Lindow, N., Shelley, M., Nazockdast, E., Kratz, A., ... & Müller-Reichert, T. (2017). C. elegans chromosomes connect to centrosomes by anchoring into the spindle network. *Nature communications*, *8*(1), 1-13.

Redemann, S., Lantzsch, I., Lindow, N., Prohaska, S., Srayko, M., & Müller-Reichert, T. (2018). A switch in microtubule orientation during C. elegans meiosis. *Current Biology*, *28*(18), 2991-2997.

Schaedel, L., John, K., Gaillard, J., Nachury, M. V., Blanchoin, L., & Théry, M. (2015). Microtubules self-repair in response to mechanical stress. *Nature materials*, *14*(11), 1156-1163.

Schaedel, L., Triclin, S., Chrétien, D., Abrieu, A., Aumeier, C., Gaillard, J., ... & John, K. (2019). Lattice defects induce microtubule self-renewal. *Nature physics*, *15*(8), 830-838.

Schuh, M., & Ellenberg, J. (2007). Self-organization of MTOCs replaces centrosome function during acentrosomal spindle assembly in live mouse oocytes. *Cell*, *130*(3), 484-498.

Stalling, D., Westerhoff, M., & Hege, H. C. (2005). Amira: A highly interactive system for visual data analysis. *The visualization handbook*, *38*, 749-67.

Srayko, M., Kaya, A., Stamford, J., & Hyman, A. A. (2005). Identification and characterization of factors required for microtubule growth and nucleation in the early C. elegans embryo. *Developmental cell*, *9*(2), 223-236.

Srayko, M., O'Toole, E. T., Hyman, A. A., & Müller-Reichert, T. (2006). Katanin disrupts the microtubule lattice and increases polymer number in C. elegans meiosis. *Current biology*, *16*(19), 1944-1949.

Vemu, A., Szczesna, E., Zehr, E. A., Spector, J. O., Grigorieff, N., Deaconescu, A. M., & Roll-Mecak, A. (2018). Severing enzymes amplify microtubule arrays through lattice GTP-tubulin incorporation. *Science*, *361*(6404), eaau1504.

Walczak, C. E., Zong, H., Jain, S., & Stout, J. R. (2016). Spatial regulation of astral microtubule dynamics by Kif18B in PtK cells. *Molecular biology of the cell*, *27*(20), 3021-3030.

Weber, B., Greenan, G., Prohaska, S., Baum, D., Hege, H. C., Müller-Reichert, T., ... & Verbavatz, J. M. (2012). Automated tracing of microtubules in electron tomograms of plastic embedded samples of Caenorhabditis elegans embryos. *Journal of structural biology*, *178*(2), 129-138.

Weber, B., Tranfield, E. M., Höög, J. L., Baum, D., Antony, C., Hyman, T., ... & Prohaska, S. (2014). Automated stitching of microtubule centerlines across serial electron tomograms. *PloS one*, *9*(12).

Woog, I., White, S., Büchner, M., Srayko, M., & Müller-Reichert, T. (2012). Correlative light and electron microscopy of intermediate stages of meiotic spindle assembly in the early Caenorhabditis elegans embryo. In *Methods in cell biology* (Vol. 111, pp. 223-234). Academic Press.

Yu, C. H., Redemann, S., Wu, H. Y., Kiewisz, R., Yoo, T. Y., Conway, W., ... & Needleman, D. (2019). Central-spindle microtubules are strongly coupled to chromosomes during both anaphase A and anaphase B. *Molecular biology of the cell*, *30*(19), 2503-2514.

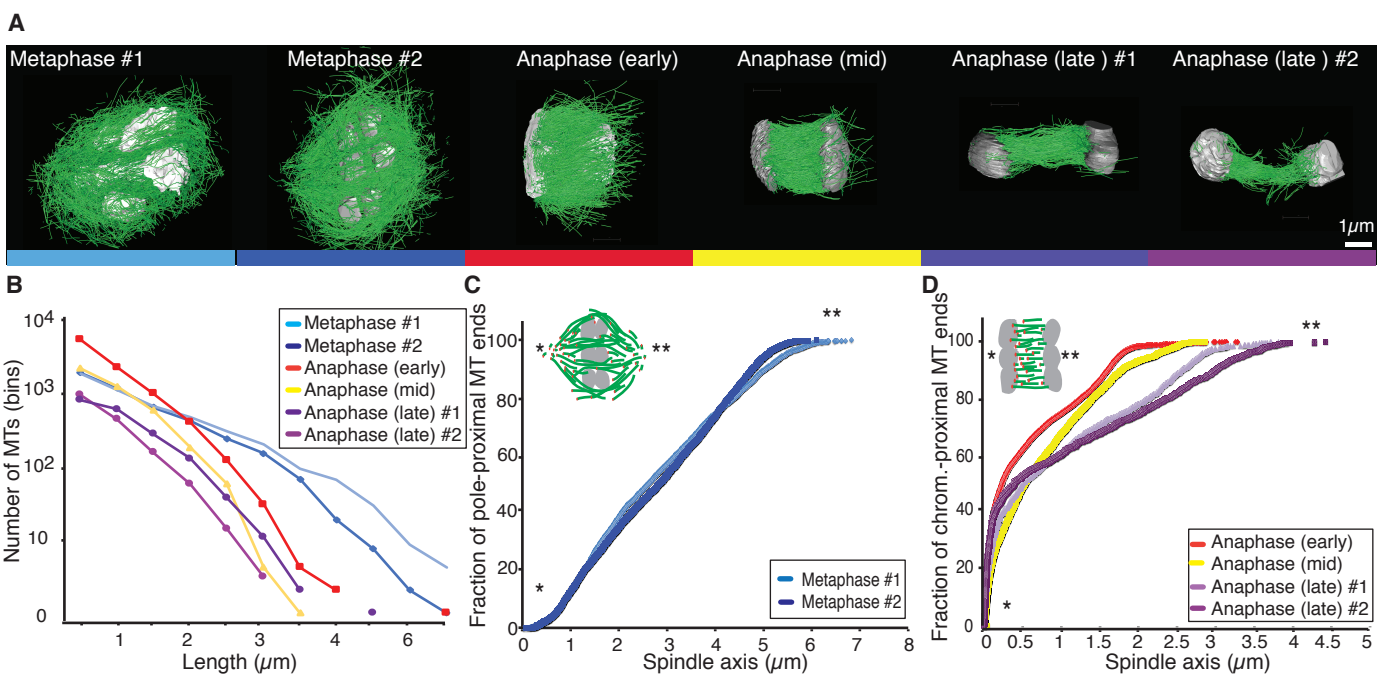
A
Metaphase #1
Metaphase #2
Anaphase (early)
Anaphase (mid)
Anaphase (late) #1
Anaphase (late) #2
1μm
B
Number of MTs (bins)
Length (μm)
Metaphase #1
Metaphase #2
Anaphase (early)
Anaphase (mid)
Anaphase (late) #1
Anaphase (late) #2
C
Fraction of pole-proximal MT ends
Spindle axis (μm)
Metaphase #1
Metaphase #2
D
Fraction of chrom.-proximal MT ends
Spindle axis (μm)
Anaphase (early)
Anaphase (mid)
Anaphase (late) #1
Anaphase (late) #2

Figure 1

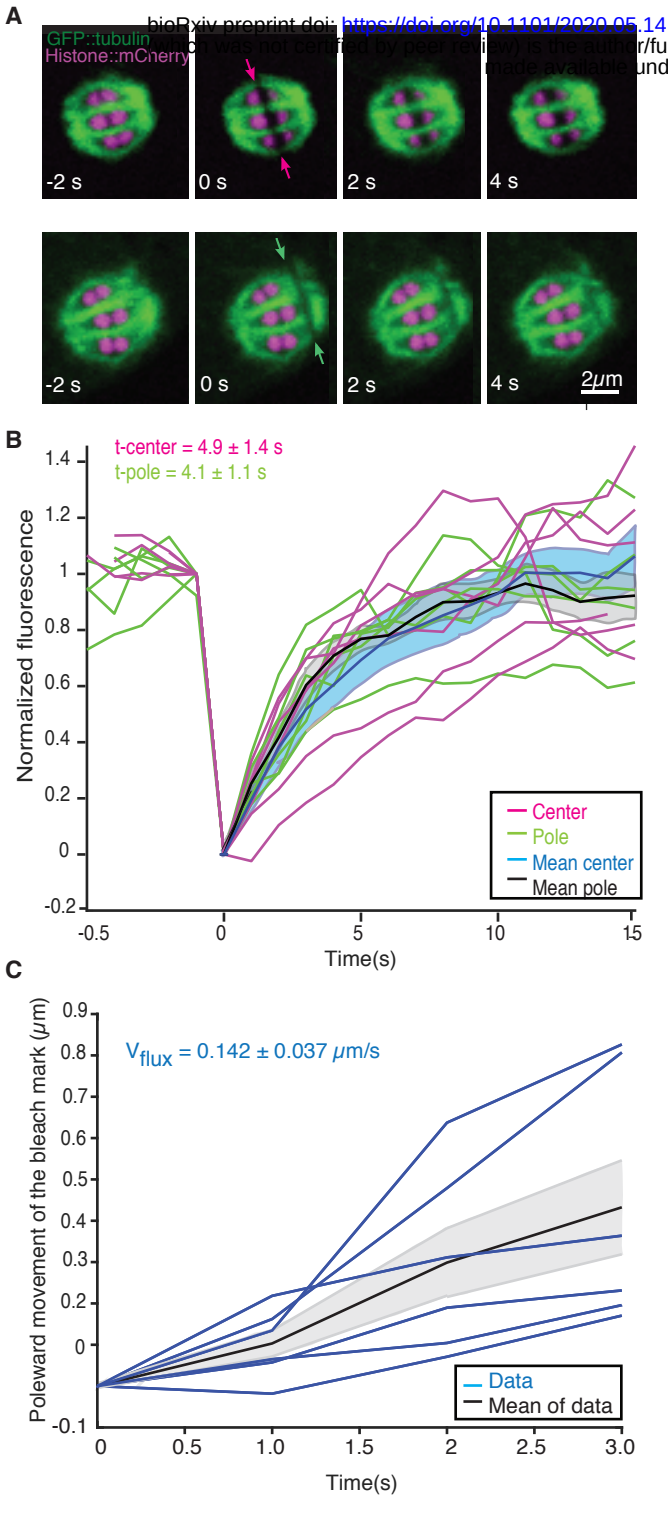

Figure 2

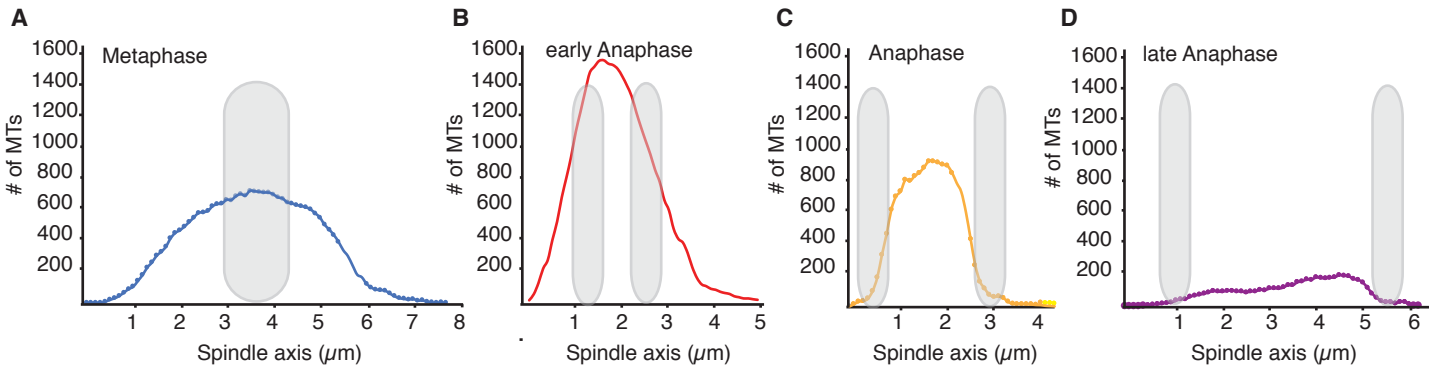
A
Metaphase
# of MTs
1600
1400
1200
1000
800
600
400
200
1
2
3
4
5
6
7
8
Spindle axis (μm)
B
early Anaphase
# of MTs
1600
1400
1200
1000
800
600
400
200
1
2
3
4
5
Spindle axis (μm)
C
Anaphase
# of MTs
1600
1400
1200
1000
800
600
400
200
1
2
3
4
Spindle axis (μm)
D
late Anaphase
# of MTs
1600
1400
1200
1000
800
600
400
200
1
2
3
4
5
6
Spindle axis (μm)

Figure 3

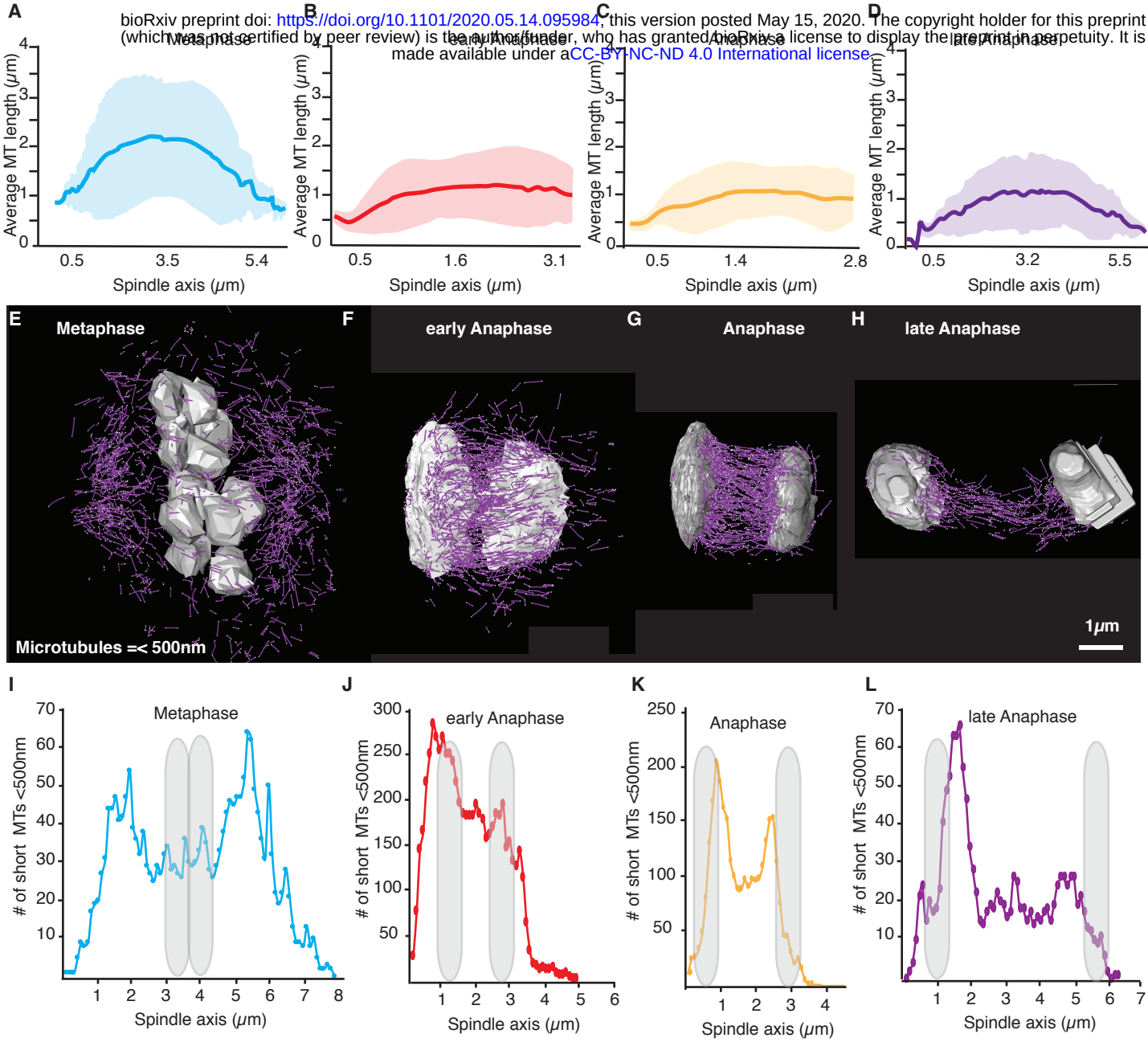

Figure 4

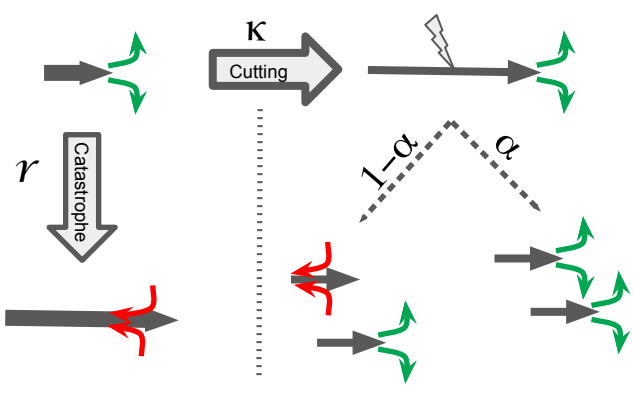

r = *turn-over* κ = *cutting rate*

α = *stability of cut microtubule plus-ends*

Figure 5

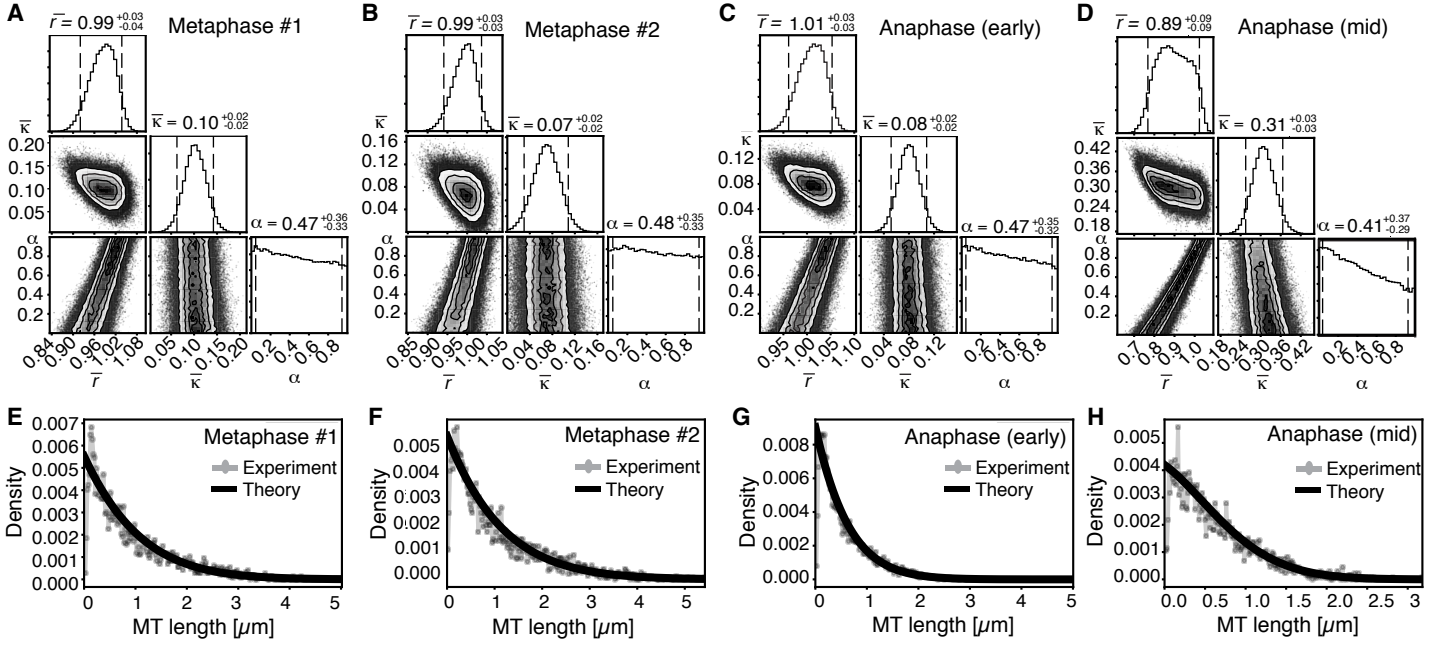
A
$\bar{r} = 0.99^{+0.03}_{-0.04}$
Metaphase #1
$\bar{\kappa} = 0.10^{+0.02}_{-0.02}$
$\alpha = 0.47^{+0.36}_{-0.33}$
B
$\bar{r} = 0.99^{+0.03}_{-0.03}$
Metaphase #2
$\bar{\kappa} = 0.07^{+0.02}_{-0.02}$
$\alpha = 0.48^{+0.35}_{-0.33}$
C
$\bar{r} = 1.01^{+0.03}_{-0.03}$
Anaphase (early)
$\bar{\kappa} = 0.08^{+0.02}_{-0.02}$
$\alpha = 0.47^{+0.35}_{-0.32}$
D
$\bar{r} = 0.89^{+0.09}_{-0.09}$
Anaphase (mid)
$\bar{\kappa} = 0.31^{+0.03}_{-0.03}$
$\alpha = 0.41^{+0.37}_{-0.29}$
$\bar{r}$
$\bar{\kappa}$
α

E
Metaphase #1
F
Metaphase #2
G
Anaphase (early)
H
Anaphase (mid)
Experiment
Theory
Density
MT length [μm]

Figure 6

	Metaphase #1	Metaphase #2	Anaphase (early)	Anaphase (mid)	Anaphase (late) #1	Anaphase (late) #2
Spindle length	5 μm	5.4 μm	3.1 μm	2.7 μm	4.5 μm	5.1 μm
Number of MTs	3662	3812	7011	3317	1511	1306
Average MT length	0.91 ± 0.08 μm	1.04 ± 0.93 μm	0.58 ± 0.52 μm	0.62 ± 0.49 μm	0.74 ± 0.54 μm	0.55 ± 0.45μm
Max. MT length	5 μm	5.4 μm	5 μm	3.2 μm	4.2 μm	2.9 μm
Net polymer length	3338 μm	3961μm	4045 μm	2061 μm	1111 μm	724 μm